CGI2015 manuscript No.
(will be inserted by the editor)

Geometric constraint-based optimization combined with physical simulation for DBS planning

Anonymous

Abstract Deep Brain Stimulation (DBS) is a neurosurgical treatment consisting in implanting an electrode in a deep structure of the brain. This kind of intervention requires millimetric accuracy in order to provide maximum therapeutic benefits, while minimizing side effects. The placement of the electrode is subjected to many rules, and computer assistance approaches including geometric constraint solving bring a valuable help in the rigorous preoperative planning of the surgery. However, mostly due to the opening of the skull at the entry point, brain tissues can deform during the surgery and alter the planning. In this paper, we present a patient-specific automatic approach for the optimization of the placement of a DBS electrode within a 3D scene of the anatomy accounting for brain deformation. Our approach combines an optimization of the position of a line within tetrahedral 3D meshes with a simulation of the deformation of the meshes by a physical model of brain shift using FEM, where the evaluated deformation depends on the candidate line and its entry point. Our method was tested successfully on a patient-specific 3D model. We will discuss the benefits of the inclusion of brain deformation estimation in our optimization framework.

Keywords Geometric constraint solving, Physically Based Modeling and Simulation, Deformable models, FEM, Optimization, Deep Brain Stimulation, Brain Shift.

1 Introduction

Methods related to computer graphics have started playing an important role in computer-assisted medical interventions. Those methods can be used for designing geometries for 3D-printed biomaterials, simulating organs to train medical students or visualizing a 3D representation of the organs structures to prepare a surgery. In this paper, we focus on the preoperative planning of a neurosurgery called *Deep Brain Stimulation* (DBS). In this introduction, we give an overview of the surgery, and emphasize the importance of pre-operative planning. It is in the critical phase that our method plays a role by using a combination of geometrical constraint and biomechanical simulation.

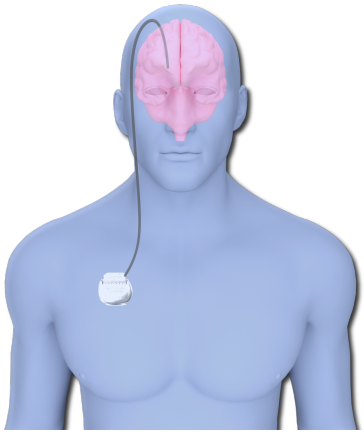

Fig. 1: DBS system: the neurostimulator, implanted in the chest, sends electrical impulses to the electrode to stimulate a deep brain structure.

DBS consists in implanting one (unilateral) or two (bilateral) permanent electrodes in the brain tissue. The goal is to continuously stimulate a disorder-specific deep nucleus of the brain using electrical impulses sent by metallic leads located at the tip of the electrode as illustrated on Fig.1. The stimulation provides to the

patient a great therapeutic benefit by removing or reducing the symptoms associated to the disorder. Most of the DBS interventions intend to treat motion disorders such as Parkinson's disease, dystonia, or essential tremors. However, it has also been successfully used for other pathologies such as chronic pain, OCD or severe depression, making it more and more popular. The reduction of the symptoms closely depends on an accurate placement of the stimulating leads at the chosen location. Because of the very small size of the target structures, the insertion of the electrode must be performed with a millimetric accuracy. Moreover, a misplacement of the electrode can lead to the stimulation of other structures in the vicinity of the target, causing side effects, or in the worst case to a massive hemorrhage if the electrode meets a vessel. To obtain the required accuracy, the surgeon performs a rigorous planning of the intervention in order to determine the location of the target and the trajectory of the electrode. The selection of the trajectory is subjected to many rules in order to ensure both the safety of the patient and the effectiveness of the procedure. This preoperative planning step is a time-consuming process which is still performed manually in most of the DBS centers.

During the surgery, a burr hole is drilled in the patient's skull in order to access the brain tissue at the entry point the surgeons defined earlier. The electrode is then inserted linearly in the direction of the target with the help of an accurate robot. When the skull and dura mater are open, cerebro-spinal fluid (CSF) can leak through the hole. This fluid surrounds the brain and support its weight. A leak of CSF may cause a change of intracranial pressure, leading to a brain deformation called *brain shift*. This phenomenon is important as brain deformation lead to a displacement of some structures, in particular the structures considered during the planning (target or obstacle structures). It results in a difference between the preoperative configuration, based on which the trajectory is selected, and the intraoperative configuration. Although the target motion can be neglected because it is located in deep tissue where the magnitude of deformation is small, blood vessels can shift up to 10 mm [8]. If a blood vessel shifts across the path of the electrode, it could lead to hemorrhage and death of the patient.

In this paper, we present a patient-specific method to compute automatically an electrode trajectory that optimizes a number of geometrical constraints and accounts for brain deformation. We combine a geometric optimization method with a physical model of the brain deformation, in order to propose a safe and effective trajectory, even in case of brain shift. In Section 2, we present works related to DBS surgical planning and brain shift modeling. Then, Section 3.1 details the physical model we use in Section 3.2 for automatically computing an optimal trajectory accounting for possible brain shift. Finally, we present our results in Section 4.

2 Related Works

Currently, most of the surgeons plan manually their intervention using some interactive medical images visualization stations, such as Medtronics StealthStation that allows them to define the target and entry points and visualize the chosen path. However, this kind of computer assistance does not spare them a long trial and error process that can take up to 1h30 for the most difficult cases.

In the last few years, various research groups have proposed solvers able to automatically compute optimal trajectories accounting for safety and efficiency [5, 9, 2, 16, 17]. Some of these approaches maximize the distance between the trajectory and obstacle structures [16], whereas others take into account a larger variety of placement rules classified into hard or soft constraints [2, 9, 17] to optimize the trajectory, and even suggest automatically a reasonable target point [5].

However, none of these approaches take into account the brain shift phenomenon. When planning manually, surgeons can roughly anticipate the motion of the structures by choosing a more posterior path. However the direction and amplitude of motion of the structure depends on several factors, such as the burr hole location or patients head orientation at the time of surgery. The objective of this work is to compute automatically an electrode trajectory which satisfies a variety of placement rules while anticipating a possible brain shift. To achieve this, we introduce an approach of automatic placement computation including an estimation of the biomechanical simulations thanks to a physical model of the brain.

When modeling the brain tissue behavior, one must make choices depending on the application. For example, a mass-spring-damper model is used in [4] to reach an update rate of 30Hz required for the training system. where the computational time must remain below 1/30 seconds to maintain interactivity. With this application, fast computation is preferred compared to accuracy. In our application, it is preferable to use a more accurate model regarding the use of the method to the preparation of a surgery. Computational time is less important, but should be reasonable to be compatible with clinical times. Most of the physics-based brain deformation models are based on the Finite Element Method (FEM), but differs from each other by

the choice of the constitutive equation. [12] and [18] use a linear constitutive equation, while [15] introduced a non-linear hyperelastic model. The law determines the tissue behavior, but there is no consensus about a constitutive equation unifying all the applications, such as simulating deformation during a car crash or a neurosurgery. Brain deformation models has been used for training systems ([4] for example), the registration of medical images ([12] and [19] for example) or compensating brain shift [3]. But they have not been widely used for the preoperative planning of a surgery. [14] use FEM to predict intra-operative brain shift, but this optimistic goal is rendered difficult due to the impossibility to predict CSF loss whereas the model relies on CSF drainage. Due to this lack of input parameters in the models, [3] pre-computed different brain deformation for possible input parameters. But the goal was to update the different structures position during the surgery. In our case, we concentrate only on the preoperative planning.

3 Methods

3.1 Brain model and brain shift simulation

In this section, we present the physical model and the numerical methods used to simulate brain shift. The first aspect is how the mechanical behavior of the brain tissue is modeled. Then, we focus on the boundary conditions which have an influence on the brain motion and deformation, and in particular the action of the cerebrospinal fluid.

3.1.1 Brain deformation

The brain is considered as a soft body subject to the laws of continuum mechanics. One of the numerical methods to solve the governing equations of motion is the Finite Element Method (FEM). In this theory, the continuum is partitioned into smaller disjoint cells called *elements*. In this work, we use $\mathcal{P}_1$ Lagrange tetrahedral elements, composed of four nodes, each with three degrees of freedom (see an example in Figure 2). The equation of motion is solved for the nodes of the element, and the values inside the element are obtained with a interpolation function defined for each node.

As the brain shift process takes place at a very low velocity, we consider the problem as quasi-static and only look for the configuration of the brain at that equilibrium, disregarding the dynamic transient effects. Finally, the discrete equation to solve is

$$\mathbf{f}(\mathbf{x}) = 0 \tag{1}$$

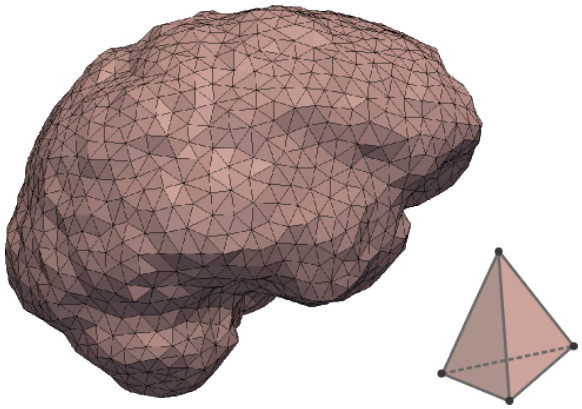

Fig. 2: Sagittal view of the tetrahedral mesh of the right hemisphere. It contains 8001 tetrahedra and 1975 nodes.

where $\mathbf{x}$ and $\mathbf{f}$ are respectively the position and the force vectors on the nodes. Here, $\mathbf{f}$ is a non-linear function of the position of the nodes $\mathbf{x}$, and represents the sum of the internal and external forces. In order to solve this non-linear equation, we use the following first-order linearization at each time step:

$$\mathbf{f}(\mathbf{x} + d\mathbf{x}) = \mathbf{f}(\mathbf{x}) + \mathbf{K}(\mathbf{x})d\mathbf{x} \tag{2}$$

where the Jacobian matrix $\mathbf{K}(\mathbf{x}) = \frac{\partial \mathbf{f}}{\partial \mathbf{x}}$ depends on the nodes position. This matrix is called *stiffness matrix* for the internal forces. The solution of Equation 1 is then approximated with the first iteration of the Newton-Raphson algorithm:

$$\mathbf{f}(\mathbf{x_n}) + \mathbf{K}(\mathbf{x_n})d\mathbf{x} = 0 \tag{3}$$

where $d\mathbf{x} = \mathbf{x} - \mathbf{x_n}$ is unknown and $\mathbf{x_n}$ is the current position. Equation 3 is a linear system solved with a Conjugate Gradient algorithm. This process is applied iteratively until reaching equilibrium.

Regarding the application of the simulation, brain deformation can be considered small. This allows us to use the Hooke's law to define the tissue behavior. It defines a linear relationship between strain σ and stress ε. For an isotropic material such as the brain, the behavior is defined by the Lamé coefficients λ and μ:

$$\sigma = 2\mu\varepsilon + \lambda \mathrm{tr}(\varepsilon) \tag{4}$$

From this law, we can write the local (relative to an element e) stiffness matrix $\mathbf{K_e}$:

$$\mathbf{K_e} = \int_{v_e} \mathbf{J_e}^T \mathbf{D_e} \mathbf{J_e} dV \tag{5}$$

where v_e is the volume of the element e, $\mathbf{J_e}$ denotes a matrix providing strain-displacement relationship and $\mathbf{D_e}$ stands for the strain-stress relation ship. In our case,

with the Hooke's law, $\mathbf{J_e}$ and $\mathbf{D_e}$ are constant. To handle large displacements (while maintaining small deformation), we use a co-rotational formulation [11], where the geometric non-linearities are approximated with the rotation of the element with respect to its initial configuration. With this approach, the stiffness matrix $\mathbf{K_e^r}$ of the element e is defined as:

$$\mathbf{K_e^r} = \mathbf{R_e}^T \mathbf{K_e} \mathbf{R_e} \tag{6}$$

where $\mathbf{R_e}$ is the rotation matrix of the element e. Finally, the global matrix $\mathbf{K}$ is assembled from the local element stiffness matrices $\mathbf{K_e}$.

3.1.2 CSF model and boundary conditions

Interaction with bony structures When the brain deforms and moves, it may collide the skull, in particular the endocranium, which is the inner surface of the skull. Once they have been detected, contacts are solved using Signorini's law:

$$0 \leq \delta \perp \lambda \geq 0 \tag{7}$$

It establishes an orthogonal relationship between the contact response force λ and the interpenetration distance δ. We ensure the Signorini's condition is fulfilled at the end of each time step by adding a term of constraints in the equation 1:

$$\mathbf{f}(\mathbf{x}) = \mathbf{H}^T \lambda \tag{8}$$

where $\mathbf{H}$ is a matrix containing the constraints directions and λ is Lagrange multipliers and contains the constraint force intensities. In Equation 8, λ is unknown and have to be computed. A linear complementary system is obtained, and is solved using a Gauss-Seidel algorithm. More details on the overall constraint solving process are given in the work [6].

Cerebro-spinal fluid The main cause of brain shift is due to a Cerebro-Spinal Fluid (CSF) loss. That is why it is indispensable to model the action of CSF on the brain. CSF is a fluid surrounding the brain, which the density is similar to water ($\rho = 1007$ kg/m^3). The loss of CSF leads to a change of the pressure inside the skull and allows the brain to deform. The action of CSF on the brain is modeled with a hydrostatic pressure:

$$\mathbf{f}_{CSF} = \int_{S_e} \big(\rho\, g\, h + p(z_0)\big) \mathrm{d}\mathbf{S} \tag{9}$$

where S_e is the surface of a submerged element belonging to the surface of the brain. g denotes the gravitational acceleration. h stands for the height from a point to the fluid surface, and $p(z_0)$ is the pressure of the point z_0 located on the fluid surface. The amount of brain shift is controlled by the fluid level. A loss of CSF corresponds to a decrease of the fluid level, therefore h decreases also, so is the fluid forces.

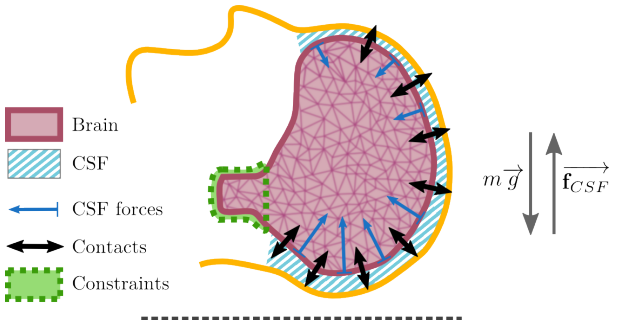

Fig. 3: Illustration showing the different components of the simulation: brain tissue is simulated with a FEM mesh, brain tissue near brainstem is anatomically constrained, CSF pressure is acting on the brain tissue and contact response in case of collision with the skull.

3.2 Trajectory planning

Our approach is inspired by the method of Essert et al. described in [9] in static conditions. We extended their approach to anticipate possible brain shift and include an estimation of the deformation within the resolution of the geometric constraints.

3.2.1 Static environment

Let us first recall briefly the approach in *static* E_S conditions. Here, the word static is used to express that the whole solving process is performed on a non-deformable 3D scene built thanks to a segmentation and 3D reconstruction of anatomical structures from preoperative MRI images using the pyDBS pipeline [7].

The resolution process consists in solving geometric constraints describing how an optimal placement for the electrode should be chosen. Two categories of geometric constraints can be found: *hard constraints* (HC) that allow to differentiate between feasible and non feasible placements, and *soft constraints* (SC) that express preferences among the feasible placements and can be mathematically represented as cost functions f_i to minimize.

All constraints are solved within a 3D scene containing 3D triangular meshes of anatomical structures, in which the objective is to locate a feasible, safe and optimal position for a ray from the skin to the target representing the trajectory of insertion of the electrode. Hard constraints are solved in a first step, consisting in eliminating from an initial portion of the mesh of the skin (Fig.4a) all the triangles that do not satisfy them all. The result of this first phase is a submesh of the initial mesh, which represents the *insertion zone* IZ_s on the skin containing all feasible *entry points*, as il-

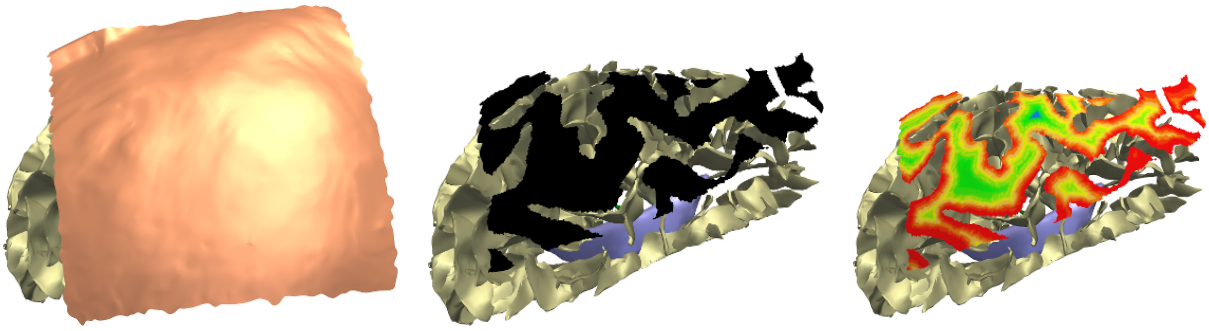

(a) Initial skin S (b) Insertion zone IZ_s (c) Color map Map_s

Fig. 4: Illustration of the different steps of the geometric constraint solving in static condition: a) initial skin mesh, b) insertion zone in black, containing only feasible entry points satisfying the hard constraints, and c) color map showing the degree of satisfaction of the soft constraints by each feasible entry point: the best zones are in blue and the worst in red

lustrated on Fig.4b. Then in a second step an aggregative cost function f, representing a weighted sum of all cost functions f_i of the n soft constraints, is minimized thanks to a derivative-free optimization algorithm such as Nelder-Mead method.

$$f = \frac{\sum_{i=1}^{n} w_i.f_i}{\sum_{i=1}^{n} w_i} \tag{10}$$

In Eq. 10, w_i are the weights expressing the relative importance of each soft constraint. They are chosen by the neurosurgeon. This second step produces a color map over the insertion zone, the colors representing the degree of satisfaction of f by each point of the insertion zone, as illustrated on Fig.4c, as well as an optimal trajectory usually located in the blue part of the color map.

Among the hard and soft constraints, the main ones concern the safety of the intervention, and involve the avoidance of surrounding anatomical structures (*obstacle meshes*) such as the sulci, where some vessels are usually located, and the ventricles. Some hard constraints allow to eliminate the triangles of the skin mesh that would lead to a collision of the ray with one of the obstacle meshes. This hard constraint is solved by using six renderings of the 3D scene from the target's point of view in the direction of the six different axis. This approach uses the GL_ARB_occlusion_query extension of OpenGL, which allows to determine the visibility of triangles of the skin's mesh by comparing the visible triangles of the mesh with and without the occluders in the scene. All occluded triangles of the skin's mesh are eliminated. This method allows for a computation of the occlusions and therefore of the safe parts of the skin in less than 2 seconds. When adding the other HC, the total computation time for IZ_s is about 12 seconds.

Some soft constraints lead the optimization towards a trajectory as distant as possible from these obstacles. The cost functions for the avoidance of the sulci and the ventricles, that are the two main obstacles the ray should avoid, are the following f_1 and f_2 respectively.

$$f_1(X) = \max\left(\frac{5 - distmin(X, sulci)}{5}, 0\right) \tag{11}$$

$$f_2(X) = \max\left(\frac{5 - distmin(X, ventricles)}{5}, 0\right) \tag{12}$$

where X is the candidate ray, and *distmin* computes the minimum distance between ray X and a 3D mesh, and *sulci* and *vessels* represent the two 3D obstacle meshes to avoid. In both cases, a minimal distance of 5 (mm) is used to prevent the ray from getting closer to the obstacle mesh.

3.2.2 Dynamic environment

In static condition, the obstacles are simply 3D triangular meshes. However, as we previously explained, a brain shift phenomenon may happen during the surgery leading to a deformation of some of the anatomical structures during the intervention which will then stabilize at a final rest position. The extent of the final deformation is hard to anticipate: for now it is not possible to determine preoperatively if the patient's brain will deform or not and what will be the exact magnitude of the deformation. However, it is possible to estimate, for a specific entry point, what would be the minimal brain shift BS_0 (corresponding to no brain shift) and maximal possible brain shift BS_{max} (corresponding to full CSF loss through the entry point), with a full range of intermediary possible deformations BS_i. Examples of possibilities are shown on Fig.5. In more intuitive words, when the patient lies on the back on the table, a burr hole close to the forehead generally produces no brain shift, whereas a burr hole in the middle of the

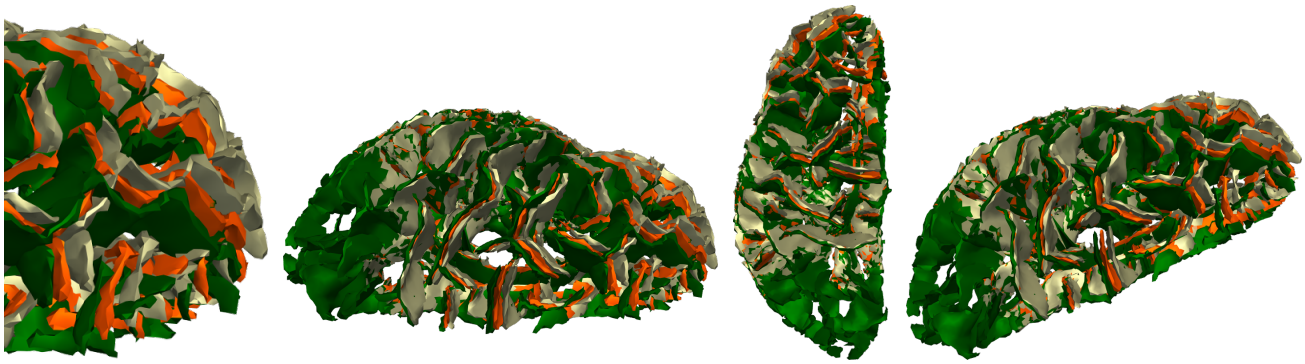

(a) Zoom (b) Sagittal (c) Axial (d) Oblique

Fig. 5: Deformation of the cortical sulci of the left hemisphere due to brain shift, in 3 different views (b to c). Only 3 deformed meshes are shown: gray mesh: no deformation, green mesh: medium deformation, and orange mesh: maximum brain shift. For readability reasons, intermediate deformed meshes are not shown. In a), a detail of the anterior part of the brain in sagittal view. Note that the difference between maximal deformed mesh and not deformed mesh is more important at the anterior part that at the posterior part.

skull is more likely to produce a maximal brain shift (as illustrated on Fig.6), but may also produce any intermediary magnitude of brain shift. Note that because of the presence of vital anatomical structures, neurosurgeons will never choose an entry point posterior to the middle of the skull.

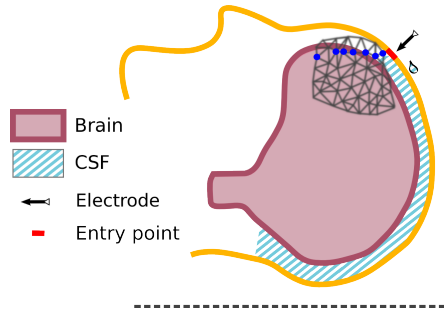

Fig. 7: Schematic representation of the entry points (blue) of the initial skin mesh S lying at the same height and likely to lead to the same possible maximal brain shift BS_h.

The purpose of the planning that we will refer to as *dynamic planning* in the rest of the paper, is to account for all possible magnitudes of brain shift that may occur based on the candidate positions of the entry point, in order to be sure to avoid the vital structures whatever their final position. Therefore, the resolution of HC and SC has to take into account the obstacle meshes not only in their initial shape, but also in the deformed shapes relative to all possible intermediary magnitudes of brain shift for each specific entry point.

An important aspect to understand in this work is that the possible range of brain shift magnitudes is different for each entry point and depends on its position on the skull which implies the maximum possible brain shift for this specific position. Therefore, whereas in static condition there was only one model of the brain M_S that was used for every computation, in deformable condition the deformed model is not unique. Several deformed models $M_{D_{CSF}}$ exist, each one corresponding to a different value of CSF loss. Each possible entry point p_i is linked to a model $M_{D_{CSF}}$ relatively to its height h on the head of the lying patient. Thanks to an interpolation with boundaries $hmax \leftrightarrow BS_0$ and $hmin \leftrightarrow BS_{max}$, it is possible to retrieve the maximum possible brain shift BS_h corresponding to height h, and therefore to the deformed model M_{D_h} that can be used with p_i. Deformed model M_{D_h} is constituted by the union of all brain shift models from BS_0 to BS_h. All points p_i lying at the same height are supposed to lead to the same possible maximum brain shift BS_h, as illustrated in Fig.7.

To achieve such a dynamic planning, we added to the 3D scene the tetrahedral meshes of the anatomical structures of the brain and used precomputed simulations of different magnitudes of brain shift from BS_0 to BS_{max}, as described in Section 3.1. It is essential to precise that the topology of the meshes do not change, and only the positions of their vertices change during the deformations.

Planning Approach. As for the planning in static condition, the dynamic planning is performed in two steps.

1. Delineation of the *insertion zone in dynamic condition* IZ_D from the skin surface mesh S by solving

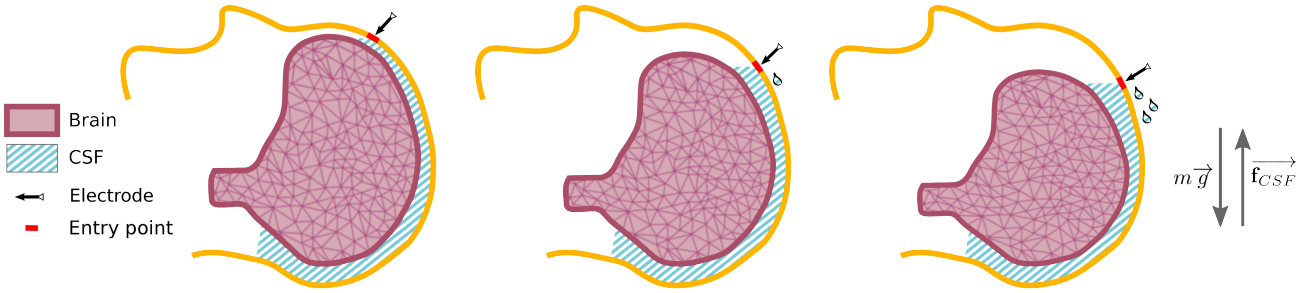

(a) High entry point (b) Medium entry point (c) Low entry point

Fig. 6: Schematic representation of the influence of the location of the entry point (red) on the loss of CSF and the possible magnitude of brain shift.

the HC. For each point $p_i \in S$ we check whether it satisfies all HC on the updated deformed model M_{D_h} corresponding to its height h and containing all possible positions of the obstacle meshes. With this approach, it was not optimal to use the GL_ARB_occlusion_query anymore for the computation of occlusion constraints, so we used instead a simple algorithm looking for the intersection between the ray X from p_i to the target point and each obstacle mesh of M_{D_h}, accelerated by OBB trees [13].

2. Compute optimal trajectory by solving the SC. We first evaluate function f described in Section 3.2.1 for each $p_i \in IZ_D$ using its corresponding deformed model M_{D_h}. Then we color IZ_D according to the values of $f(p_i)$ to obtain a dynamic risk map Map_S. In the same way, the evaluation of SC is done on the updated model M_D. Finally, we identify the most interesting point in IZ_d, and optimize it more accurately using a local derivative-free optimization algorithm (Nelder-Mead method). At each iteration of the optimization algorithm, a new candidate trajectory is proposed. Its deformed model M_{D_h} is determined based on its corresponding insertion point, and function f is evaluated. The optimization algorithm stops when the improvement of f falls under a threshold ε.

The overall algorithm including the two steps is detailed in Algorithm 1.

Algorithm 1: Dynamic Planning Algorithm

Data: M_S: Initial 3D model of patient's brain
S: Initial skin mesh
Sim_{DB}: Patient's simulations file
HC and SC: Hard and Soft constraints
Result: T: Optimal trajectory in E_D
Map_D: Dynamic risk color map

$IZ_d \leftarrow \emptyset$; $Map_d \leftarrow \emptyset$; $ST \leftarrow \emptyset$;
/*Resolution of Hard Constraints HC*/
foreach $p_i \in S$ **do**
  $h \leftarrow getHeight(p_i)$;
  $M_{D_h} \leftarrow \bigcup_{i=0 \rightarrow h} BS_i$;
  if $satisfy(p_i, HC, M_{D_h})$ **then**
    $IZ_D \leftarrow IZ_D \cup p_i$;
/*Resolution of Soft Constraints SC*/
/*Computation of Color Map*/
foreach $p_i \in IZ_D$ **do**
  $h \leftarrow getHeight(p_i)$;
  $M_{D_h} \leftarrow \bigcup_{i=0 \rightarrow h} BS_i$;
  $eval\_table \leftarrow evaluate(p_i, SC, M_{D_h})$;
$Map_D \leftarrow color\_insertion\_zone(IZ_D, eval\_table)$;
/*Computation of Optimal Trajectory*/
$T \leftarrow extract\_best\_solution(Map_D)$;
$prev\_eval = 1$;
$h \leftarrow getHeight(T)$;
$M_{D_h} \leftarrow \bigcup_{i=0 \rightarrow h} BS_i$;
$eval \leftarrow f(T)$;
while $prev\_eval - eval > \varepsilon$ **do**
  $T \leftarrow propose\_new\_candidate(NelderMead, IZ_D)$;
  $prev\_eval \leftarrow eval$;
  $h \leftarrow getHeight(T)$;
  $M_{D_h} \leftarrow \bigcup_{i=0 \rightarrow h} BS_i$;
  $eval \leftarrow f(T)$;

Overview of the system. Our system is illustrated in Fig.8. It is composed of two main units: planning and simulation, and uses other third-party frameworks such as pyDBS, SOFA, and MITK. First of all, we use pyDBS pipeline [7] to reconstruct a patient-specific 3D surface model of the brain from intraoperative MRI scans of the head. The tetrahedral meshes of the structures involved in the brain shift deformation are generated using CGAL library [1]. The biomechanical simulations are performed within the SOFA framework [10]. For each input patient model, a set of deformed brain models is precomputed using simulations. They correspond to the different magnitudes of possible brain shift from a minimum to the maximum. We store all the intermediary deformed models and consider them as a patient-specific simulations database. The interest of

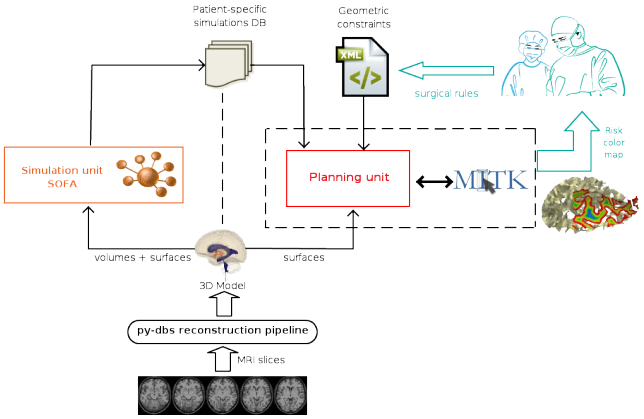

Fig. 8: Overview of the system

using precomputed simulations is to save computational time during the optimization process, and to allow to run several consecutive constraint resolutions with different settings without the need to perform new simulations. On the planning side, the solver we implemented to optimize the electrode trajectories takes as an input a set of surgical rules described by neurosurgeons and formalized as geometric constraints in XML syntax (HC and SC). The constraints file is not patient-specific, and is only related to the description of the DBS intervention, which makes it easy to upgrade in case new rules are discovered. The other inputs of the planning unit are the surfaces from pyDBS, the corresponding simulations database, and the geometric constraint file. The planning unit computes a patient's color map accounting for possible deformations, and proposes it to the surgeon in an interactive interface with many display facilities. The DBS surgical planning plugin is developed based on MITK framework [20].

4 Experimental Results

4.1 Experiment

We tested our approach on a patient-specific 3D model from a retrospective case. The model consists of 3D triangular surface meshes of the sulci, ventricles, subthalamic nucleus, and a skin patch of the scalp.

The tetrahedral mesh of the brain is generated from the binary image provided by pyDBS, where intensities indicate if the voxels belong to the brain tissue. In addition, the simulation needs the surface mesh of the interior of the skull. This can be extracted from a preoperative CT scan, usually performed in clinical routine. The sulci contain most of the blood vessels which are difficult to segment, and therefore they are considered as a geometric obstacle to be avoided during the planning. The ventricles represent another risky anatomical structure which should be avoided as well, while the center of the subthalamic nucleus is the anatomical target.

During the planning phase, the skin patch is our initial solution space. The number of elements in the complete surface model is 83k., and the dimensions of the bounding box of the target mesh are $12 \times 9 \times 4$ mm. The planning was performed on an Intel Core i7 running at 2.67 GHz with 8GB RAM workstation. The patient-specific simulations DB contains 20 simulated brain shift levels. The simulations were run on an Intel Core i7 running at 2.7 GHz with 8GB RAM laptop. The number of tetrahedral elements and associated nodes are given in Fig. 2. The mechanical parameters are set to $\lambda = 1291$ Pa and $\mu = 1034$ Pa according to [12].

Our experiments consists in comparing the new method in E_D with the previous one in E_S, mainly on two aspects: to compare the feasible insertion zones, and see the efficiency of the optimization approach. Therefore, we applied the same test in both environments and we reported the obtained results.

4.2 Results

4.2.1 Feasible insertion zones

In Table 1 we compare the insertion zones sizes, computation times, and the ratio of the size of the insertion zone compared to the initial skin patch.

Table 1: Computation of the insertion zones: resulting size and computation times

	S	IZ_S	IZ_D
# Triangles	67920	17408	7868
Comp. time (s)	-	12	36
S coverage %	100	25.6	11.6

First of all, we notice that as we expected IZ_D is smaller than IZ_S which is due to the larger number of obstacles in deformable condition. Fig.9 shows the initial skin patch S, with the two insertions zones (static IZ_S and dynamic IZ_D). It can also be noticed that the percentage of IZ_D to IZ_S is equal to %45.2 which means that the feasible insertion zone is reduced by %54.8. This means that if the possible deformation due to brain shift is not taken into account in the planning, up to one half of the insertion zone mesh actually contains dangerous entry points in case of brain shift.

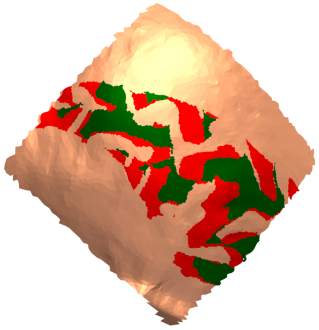

Fig. 9: S is the large orange patch, IZ_S is a subset of S and is the union of red and green shapes, and IZ_D is a subset of IZ_S and is the green mesh.

The required time to build IZ_D is around 36 s which is 3 times higher than the time required to build IZ_S, but still keeps the approach compatible with clinical use. The time needed to build the color map is equal to 5 s in E_S and to 31 s in E_D.

In this experiment, we tried different refinements of the initial mesh S. Finally, in the tested model the number of triangles was increased from 4245 to 67920 by implementing a deep subdivision to obtain a more precise color map.

The average time of a single simulation is equal to 1 minute. This emphasizes the interest of precomputing the simulations, to avoid to slow the planning down and allow for several runs with different settings.

4.2.2 Nelder-Mead optimization

Table 2 shows the performance of Nelder-Mead optimization algorithm in both E_S and E_D. We report the value of the evaluation of cost function f which we are minimizing, the distance between the optimized ray and the obstacle meshes (ventricles and sulci), then we show the number of iterations and convergence time. At last, the number of maximum deformation levels employed by the optimizer within the candidate points range.

Table 2: Nelder-Mead performance in E_s and E_d

Nelder-Mead	E_S	E_D
eval(f) $[0, 1]$	0.28	0.38
dist. from ventricles (mm)	11.87	7.39
dist. from sulci (mm)	5.13	3.12
# of iterations	31	21
time (s)	0.034	0.258
# of h levels used	-	3

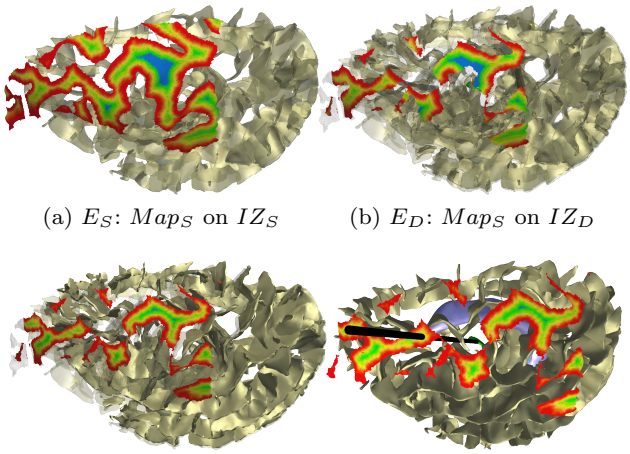

(a) E_S: Map_S on IZ_S (b) E_D: Map_S on IZ_D

(c) E_D: Map_D on IZ_D (d) E_D: Optimal trajectory

Fig. 10: A risk map built in a static environment and superimposed on a static insertion zone (a) does not remain correct when it overlays on a dynamic insertion zone (b). The dynamic risk map is shown in (c).

The values in Table 2 show that the optimization algorithm used in E_S could also converge in E_D, and give an acceptable proposition for trajectory T that is sufficiently secure for DBS even in case of brain shift. The optimized trajectory in E_D was closer to the obstacles than the one in E_S but it could remain far enough from them. The resulting optimal trajectory in E_D is shown on Fig.10d.

Consequently, the best evaluation value in E_D (0.38) was not as good as the best one in E_S(0.28) but still acceptable. The optimization time is negligible in both cases. The number of brain shift magnitudes used in the optimization phase was just 3. This is because the optimization starts in an already interesting position, and the local optimization does not go far from that initial guess. The influence of the number and density of the simulations will be discussed in the next section.

Another interesting outcome we obtain after optimization is the fact that the best insertion regions (blue zones) on Fig.10 in static condition are not necessarily the best insertion regions in the dynamic one.

5 Conclusion

The obtained results show the variation of the safe feasible insertion zones for DBS interventions between the static and the dynamic conditions. This variation shows the interest of including the brain shift deformation during the planning phase, as it removes dangerous entry points that would not be detected otherwise. Although avoiding a sum of deformations from no brain-

shift to a maximum possible brain-shift causes a high restriction of the feasible insertion zone, the remaining insertion zone could still provide an optimized entry point which is safe and efficient.

The implemented optimization algorithm performed well in our test. However, we think that other categories of optimization algorithms could be implemented and compared. One advantage of our modular system is that the simulations time is kept aside from the optimization time. In clinical routine, they could be precomputed just after acquiring the patient's MRI, and before the surgeon interacts with the planning software.

We also think that increasing the simulations number in the patient-specific simulations DB could lead to a more precise planning.

We presented a novel approach for DBS automatic preoperative planning. We coupled physical simulations with geometric constraint-based optimization to help the surgeon to anticipate the possible deformation during the planning. We tested our system on a patient-specific 3D model, with very promising results.

However, further work could be done to improve the system. Other optimization techniques could be investigated. We would also like to improve the accuracy of the brain shift model by using more complex deformation and fluid models, while maintaining similar computational times. Moreover, we need to measure the influence of the equation governing brain deformation and its parameters on the final resulting planning. Finally, clinical validation is required to test the robustness of the overall system, through a measurement of the effects of this new method on the safety and effectiveness of the procedure.

References

1. CGAL, Computational Geometry Algorithms Library. Http://www.cgal.org
2. Bériault, S., Subaie, F., Mok, K., Sadikot, A., Pike, G.: Automatic trajectory planning of DBS neurosurgery from multi-modal MRI datasets. In: proceedings of MICCAI'11, *Springer LNCS*, vol. 6891, pp. 259–266 (2011)
3. Chen, I., Coffey, A.M., Ding, S., Dumpuri, P., Dawant, B.M., Thompson, R.C., Miga, M.I.: Intraoperative brain shift compensation: accounting for dural septa. IEEE transactions on bio-medical engineering **58**(3), 499–508 (2011)
4. De Paolis, L.T., De Mauro, A., Raczkowsky, J., Aloisio, G.: Virtual model of the human brain for neurosurgical simulation. Studies in health technology and informatics pp. 811–815 (2009)
5. D'Haese, P.F., Pallavaram, S., Li, R., Remple, M.S., Kao, C., Neimat, J.S., Konrad, P.E., Dawant, B.M.: Cranial-vault and its crave tools: A clinical computer assistance system for deep brain stimulation (DBS) therapy. Medical Image Analysis **16**(3), 744–753 (2012)
6. Duriez, C., Cotin, S., Lenoir, J., Neumann, P.: New approaches to catheter navigation for interventional radiology simulation. Computer Aided Surgery **11**(6), 300–308 (2006)
7. DAlbis, T., Haegelen, C., Essert, C., Fernandez-Vidal, S., Lalys, F., Jannin, P.: Pydbs: an automated image processing workflow for deep brain stimulation surgery. International journal of computer assisted radiology and surgery pp. 1–12 (2014)
8. Elias, W.J., Fu, K.M., Frysinger, R.C.: Cortical and subcortical brain shift during stereotactic procedures. Journal of neurosurgery **107**(5), 983–8 (2007)
9. Essert, C., Haegelen, C., Lalys, F., Abadie, A., Jannin, P.: Automatic computation of electrode trajectories for deep brain stimulation: a hybrid symbolic and numerical approach. International journal of computer assisted radiology and surgery **7**(4), 517–532 (2012)
10. Faure, F., Duriez, C., Delingette, H., Allard, J., Gilles, B., Marchesseau, S., Talbot, H., Courtecuisse, H., Bousquet, G., Peterlik, I., Cotin, S.: SOFA: A Multi-Model Framework for Interactive Physical Simulation. In: Y. Payan (ed.) Soft Tissue Biomechanical Modeling for Computer Assisted Surgery, *Studies in Mechanobiology, Tissue Engineering and Biomaterials*, vol. 11, pp. 283–321. Springer (2012)
11. Felippa, C., Haugen, B.: A unified formulation of small-strain corotational finite elements: I. theory. Computer Methods in Applied Mechanics and Engineering **194**(21), 2285–2335 (2005)
12. Ferrant, M., Nabavi, A., Macq, B., Black, P.M., Jolesz, F.a., Kikinis, R., Warfield, S.K.: Serial registration of intraoperative MR images of the brain. Medical image analysis **6**(4), 337–59 (2002)
13. Gottschalk, S., Lin, M.C., Manocha, D.: Obbtree: A hierarchical structure for rapid interference detection. In: Proc. of the 23rd annual conference on Computer graphics and interactive techniques, pp. 171–180. ACM (1996)
14. Hu, J., Jin, X., Lee, J.B., Zhang, L., Chaudhary, V., Guthikonda, M., Yang, K.H., King, A.I.: Intraoperative brain shift prediction using a 3D inhomogeneous patient-specific finite element model. Journal of neurosurgery **106**(1), 164–9 (2007)
15. Miller, K., Chinzei, K.: Mechanical properties of brain tissue in tension. Journal of biomechanics **35**, 483–490 (2002)
16. Shamir, R., Tamir, I., Dabool, E., Joskowicz, L., Shoshan, Y.: A method for planning safe trajectories in image-guided keyhole neurosurgery. In: proceedings of MICCAI'10, vol. 6363, pp. 457–464. Springer LNCS (2010)
17. Tirelli, P., de Momi, E., Borghese, N., Ferrigno, G.: An intelligent atlas-based planning system for keyhole neurosurgery. In: Computer Assisted Radiology and Surgery supplemental, pp. S85–S91 (2009)
18. Škrinjar, O., Spencer, D., Duncan, J.S.: Brain shift modeling for use in neurosurgery. Proceedings of MICCAI98 (1998)
19. Wittek, A., Joldes, G., Couton, M., Warfield, S.K., Miller, K.: Patient-specific non-linear finite element modelling for predicting soft organ deformation in real-time: application to non-rigid neuroimage registration. Progress in biophysics and molecular biology **103**(2-3), 292–303 (2010)
20. Wolf, I., Vetter, M., Wegner, I., Bttger, T., Nolden, M., Schbinger, M., Hastenteufel, M., Kunert, T., Meinzer, H.P.: The medical imaging interaction toolkit. Medical Image Analysis **9**(6), 594–604 (2005)